

Algorithms for correcting geometric distortions in delay line anodes

Erik Wilkinson^a, Steven V. Penton^a, Stephané Béland^a, John V. Vallerga^b,
Jason McPhate^b, David J. Sahnow^c

^aCenter for Astrophysics and Space Astronomy
University of Colorado, Boulder, CO 80309

^bSpace Sciences Laboratory
University of California, Berkeley, CA 94720

^cDepartment of Physics and Astronomy
Johns Hopkins University, Baltimore, MD 21218

ABSTRACT

Time-delay anodes are typically used in conjunction with microchannel plates to provide photon counting and two-dimensional imaging. The anode and associated electronics are used to compute the centroid of the charge cloud from the microchannel plate stack. The computation is done in analog circuitry and reported as a digital value.

The analog nature of the time-delay anode makes them susceptible to variations in the correlation between physical space and the reported digital value. These variations, both local and global, must be corrected as part of the data reduction of scientific data. If left uncorrected in spectral data, for example, these variations would result in inaccurate wavelength identifications and distorted spectral line profiles.

This work describes successful algorithms for correcting the dominant distortions present in a time-delay anode; geometric (local) and thermal (global) distortions. These algorithms were developed as part of the data reduction pipelines for the Cosmic Origins Spectrograph (COS), a fourth generation instrument for the Hubble Space Telescope, and the Far Ultraviolet Spectroscopic Explorer (FUSE).

Keywords: Detectors, readouts, delay-line anodes, distortion correction, microchannel plates, ultraviolet

1. INTRODUCTION

In a scientific instrument the detector is often the most important component for it is ultimately the source of the data. Understanding how the detector interprets the incident radiation is crucial to understanding the performance of the instrument as a whole.

The dominant detector in extreme- and far-ultraviolet astronomy today is the microchannel plate (MCP) detector. MCP detectors have flown on a host of major satellite missions including EUVE¹, IMAGE², SOHO³, HST⁴, and FUSE⁵, and a wide range of sounding rocket experiments⁶. A MCP detector consists of two parts, the MCP stack and the readout device. The MCP stack is responsible for converting the incident photon into a cloud of 10^5 - 10^{10} electrons. The centroid of the electron cloud is, for this discussion, assumed to be also the location of the incident photon to within the pore spacing of the top MCP in the stack. The readout device, or anode, and supporting electronics are responsible for determining the centroid of the charge cloud and thus the coordinates of the incident photon.

There are several continuous and digitized anode schemes available today. In a digital readout there is a direct correlation between a physical region on the anode and the reported digital location. This relationship is fixed by structures on the anode and does not change. Digital readouts include the multi-anode microchannel array⁷ (MAMA), the coded anode converter^{8,9} (CODACON), and the oblique imager converter, flown on the IMAPS¹⁰ instrument.

A continuous readout, on the other hand, computes the centroid of the charge cloud in analog circuitry. The analog value of the centroid is then digitized. Examples of continuous readouts include resistive anodes^{11,12}, wedge and strip¹³, vernier anodes¹⁴, and time delay anodes^{15,16,17}. Depending upon the exact implementation of the electronics, these readout schemes can support count rates of up to 500 kHz with resolutions of between 20 μm and 100 μm . A

disadvantage of continuous readout devices is that since the position of an event is computed in the analog circuitry, the relationship between physical space and the reported pixel value is susceptible to a host of outside influences including temperature, noise on the ground and power lines, and count rate. It is these effects and how to compensate for them that is the focus of this work.

This work is largely motivated by two ultraviolet satellite missions; the Far Ultraviolet Spectroscopic Explorer¹⁸ (FUSE), which has been operating since June 1999, and the upcoming Hubble Space Telescope Cosmic Origins Spectrograph¹⁹ (HST/COS), due to be installed in late 2003 during Servicing Mission 4. Both satellite missions are spectroscopic missions designed to acquire high-resolution ($\lambda/\Delta\lambda \sim 20-30,000$) spectra in the far ultraviolet (900-1180Å, FUSE; 1150-1775Å, COS). Both optical designs rely on large format, microchannel plate detectors with time delay anodes and challenging resolution requirements of 20-30 μm full width half maximum (FWHM). The FUSE and COS detectors consist of two 85mm X 10mm (16384 X 1024 pixels) segments oriented to provide ~200mm X 10mm active area.

The detectors for FUSE and COS were developed and built by the Experimental Astrophysics Group at the University of California, Berkeley. Each detector employs time delay electronics to measure the position of an event along the dispersion axis. Measurement of the y coordinate in the FUSE detector was computed using charge division¹³ while COS utilizes a second time delay line anode (The COS anode is referred to as a cross-delay line (XDL) anode). A significant amount of effort has been expended by the FUSE and COS teams to understand how to correctly reduce the data from these detector systems. This work presents in detail two successful algorithms for correcting the data for thermal (global) and geometric (local) distortions.

In section two we discuss how a time delay anode computes the location of a valid event. Section three discusses how global variations in the data are introduced and how to correct them. Section four focuses on localized variations in the plate scale and how to correct them. Conclusions are presented in section 5.

2. THE TIME-DELAY ANODE

2.1 Functional Description of a Time-Delay Anode

A time-delay anode and associated electronics compute the centroid of a charge cloud by measuring the difference in arrival time between pulses traveling in opposite directions along the anode. After the charge cloud from the microchannel plate stack impacts the conductive traces on the anode it splits into two charge pulses traveling in opposite directions. One charge pulse, the “begin” signal, initiates the discharge of a precision capacitor. The discharge is halted by the arrival of the second charge pulse, the “end” signal (see Figure 1). The remaining voltage on the capacitor is thus directly proportional the position of the detected event. An analog-to-digital converter (ADC) converts the voltage on the capacitor into a digital value.

Mathematically the reported position of an event can be expressed as follows:

Definitions:

x	-	position on anode (mm)	t_0	-	time of event
t_b	-	time of “begin” signal	t_e	-	time of “end” signal
t_d	-	extra delay	Δt	-	time difference measured by TDC
ϵ_c	-	capacitor dielectric constant	ϵ_a	-	anode dielectric constant
v_a	-	anode signal velocity	D	-	anode length
I	-	integrator current	C	-	integrator capacitance
V	-	integrator voltage	V_0	-	integrator offset
A	-	ADC conversion gain	P_0	-	ADC offset
P	-	pixel position			

In a delay-line detector, the x or y dimension is determined by measuring the time difference assuming the anode velocity is constant. For an event at time t_0 on the anode at position x (zero point arbitrarily defined at the center of the anode), the times of arrival at the ends of the anode are:

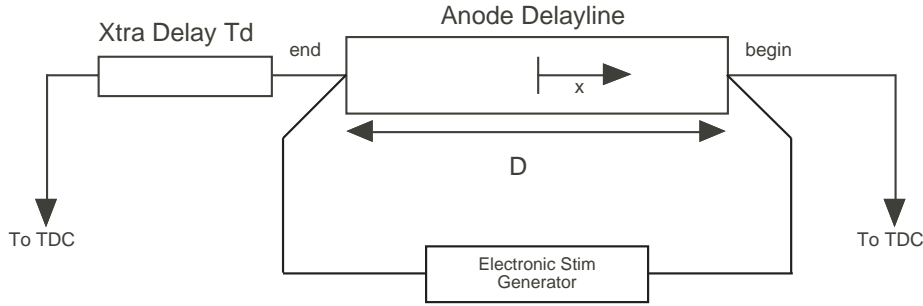


Figure 1: Schematic representation of the time-delay anode and electronic stim circuit.

$$t_b = \frac{(D/2 - x)}{v_a} \quad (1)$$

$$t_e = t_d + \frac{(D/2 + x)}{v_a} \quad (2)$$

$$x = v_a \frac{(t_e - t_b)}{2} \quad (3)$$

An arbitrary time delay t_d is added to the signal coming out of one side of the anode such that the "begin" signal always leads the "end" signal.

$$\Delta t = t_e - t_b = \frac{(D/2 + x)}{v_a} - \frac{(D/2 - x)}{v_a} + t_d = \frac{2x}{v_a} + t_d \quad (4)$$

The time difference is measured by a current integrator where a constant current, I , is directed into a capacitor, C , for a time Δt resulting in a voltage out, V .

$$V = I \frac{\Delta t}{C} + V_o \quad (5)$$

An ADC with conversion gain A (pixels/volt) converts this voltage into a digital value P . Both the integrating capacitor and ADC can have residual offsets, V_o and P_o .

$$P = AV + P_o = AI \frac{\Delta t}{C} + AV_o + P_o \quad (6)$$

$$P(x) = AI \frac{(2x/v_a)}{C} + AI \frac{t_d}{C} + AV_o + P_o \quad (7)$$

A key feature in both FUSE and COS detectors is an onboard system for monitoring the variations in performance that occur over time and temperature. The system works by injecting a small amount of charge at the two ends of the time-delay anode itself, thus introducing "events" outside the area defined by the microchannel plate active area. These events are referred to as electronic stim pulses or "e-stims", as they are an electronic implementation of physical stimulation pins used on other detectors. Figure 1 shows a schematic representation of the electronic stimuli and Figure 2 shows the locations of the e-stims with respect to the active and digital areas defined by the anode for the COS detector. Any change in the performance of the delay-line anode itself or the analog portion of the supporting electronics will change the location of the e-stims. By tracking the locations of the e-stims, it is possible to compensate for the temperature dependent variations in the mapping between digital to physical space.

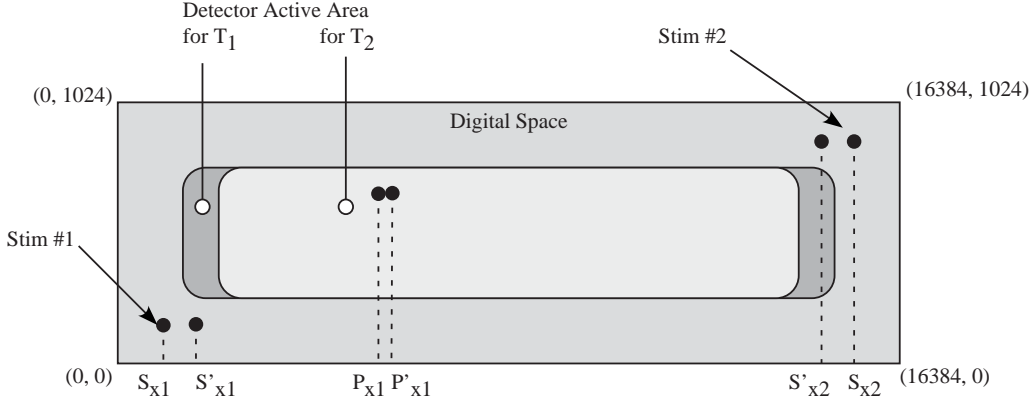


Figure 2: Schematic representation of a single segment of the COS detector showing the locations of the e-stims with respect to the digital space and microchannel plate active area. T_1 and T_2 refer to two different temperatures.

2.2 Performance variations in delay-line anode detectors

The major cause of image shift in COS XDL anodes and the FUSE double-delay line anodes is due to the temperature dependence of the dielectric constant, ϵ_a , of the anode substrate material (RT Duroid) and to a smaller extent, the dielectric constant of the integrating capacitor, ϵ_c . The anode signal propagation velocity is inversely proportional to the square root of the anode dielectric constant, ($v_a \propto \epsilon_a^{-1/2}$), while the capacitance of the integrating capacitor is directly proportional to its dielectric constant ($C \propto \epsilon_c$).

Using the e-stim positions ($x=\pm D/2$) it is possible to determine both the slope and y-intercept of the plate scale of the detector, as is shown in equations 8 through 11, and to demonstrate how they are affected by the dielectric constant of the anode and the capacitance of the integrating capacitor. Equations 8 and 9 are the locations of the e-stims and equations 10 and 11 are the slope and y-intercept respectively.

$$P(D/2) = A I \frac{t_d}{C} + AV_0 + P_0 + A I \frac{D}{v_a C} \quad (8)$$

$$P(-D/2) = A I \frac{t_d}{C} + AV_0 + P_0 - A I \frac{D}{v_a C} \quad (9)$$

$$P(D/2) - P(-D/2) = 2 A I \frac{D}{v_a C} \text{ (slope)} \quad (10)$$

$$\left(\frac{P(D/2) + P(-D/2)}{2} \right) = A I \frac{t_d}{C} + AV_0 + P_0 \quad (\text{y-intercept, } x = 0) \quad (11)$$

Equations 10 and 11 demonstrate that as the temperature changes the plate scale ($\mu\text{m/pixel}$) and the offset (pixels) also change. Thus, the reported pixel for a photon incident onto a fixed point on the active area of the MCPs will be different depending upon the temperature of the electronics. This makes it impossible to directly co-add data sets or reference flight data to calibration data without a loss in resolution, because there is no correlation between physical position and pixel values. Understanding and correcting for this difference between pixel and physical location is the first and most important step in producing a high quality data set.

3. CORRECTING THERMAL DISTORTIONS

The variation of the global plate scale is uniform across the anode, assuming that the anode is isothermal. The expression for mapping the position of any detected photon at an arbitrary pixel scale (i.e. arbitrary temperature) to its physical position in a common reference frame (CRF) using the electronic stim locations is derived below. In this

derivation the assumption is that we are converting an arbitrary data set into a CRF as defined by two specific locations of stim centroids.

Definitions (refer to Figure 2):

X	– physical location of a detected photon in microns.
T_1	– temperature 1
T_2	– temperature 2
S_{x1}	– the centroid (pixels) of the left-hand e-stim in the dispersion direction at temperature T_1 (calibration constant that defines the CRF).
S_{x2}	– the centroid (pixels) of the right-hand e-stim in the dispersion direction at temperature T_1 (calibration constant that defines the CRF).
S'_{x1}	– the centroid (pixels) of the left-hand e-stim in the dispersion direction at temperature T_2 .
S'_{x2}	– the centroid (pixels) of the right-hand e-stim in the dispersion direction at temperature T_2 .
a	– the X offset in microns at T_1 .
a'	– the X offset in microns at T_2 .
b	– the pixel scale in microns/pixel at T_1 .
b'	– the pixel scale in microns/pixel at T_2 .
P_x	– pixel value of the photon at T_1 .
P'_x	– pixel value of the photon at T_2 .

At T_1 the position X of a photon is described by Equation 12,

$$X = a + bP_x \quad (12)$$

and at T_2 by equation 13;

$$X' = a' + b' P'_x \quad (13)$$

The electronic stims remain fixed in physical space, so $X = X'$ for an e-stim. Therefore, we can solve for a and b at all times using the electronic stim locations. The solution goes as follows:

At $X = X'$ we have for each e-stim location;

$$a + bS_{x1} = a' + b'S'_{x1} \quad (14)$$

$$a + bS_{x2} = a' + b'S'_{x2} \quad (15)$$

Solving for a' and b' we find;

$$a' = a + bS_{x1} - b'S'_{x1} \quad (16)$$

$$b' = b \frac{S_{x2} - S_{x1}}{S'_{x2} - S'_{x1}} \quad (17)$$

Given the centroid of the e-stims at any given time, any photon can be mapped to a fixed position in physical space using equation 12. Combining Equations 13, 16, and 17 results in Equation 18.

$$X' = a + b \left[S_{x1} + \frac{(S_{x2} - S_{x1})}{(S'_{x2} - S'_{x1})} (P'_x - S'_{x1}) \right] \quad (18)$$

X' must now be converted back into units of pixels at temperature T_1 ($X' \equiv X$), so equating Equation 18 to Equation 12 and solving for P_x we get Equation 19, which is the pixel value for a photon detected at temperature T_2 in the pixel scale at T_1 .

$$P_x(P'_x) = S_{x1} + (P'_x - S'_{x1}) \frac{(S_{x2} - S_{x1})}{(S'_{x2} - S'_{x1})} \quad (19)$$

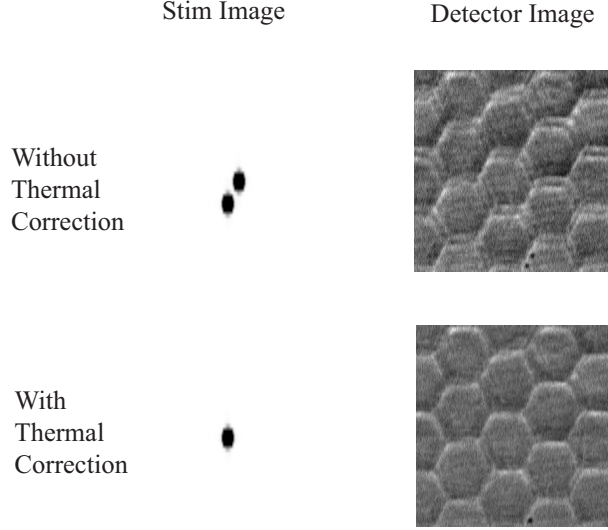


Figure 3: The upper panels show the electronic stimulations and resultant image of two images added without alignment to a common reference frame (CRF). The lower images have been aligned to a CRF. Notice how the clarity, and ultimately the resolution, of the image is improved by correcting the image for thermal distortions.

Figure 3 shows images of the e-stims before and after thermal corrections have been applied. The upper left panel of Figure 3 shows images of e-stims for two images at slightly different temperatures. If the images were co-added without alignment to the CRF, the image would be blurred, as shown in the upper right panel. Without co-alignment to the CRF, the effective resolution of the data set is decreased. If, however, the e-stims are aligned to the CRF (lower left panel of Figure 3), the resultant co-addition is noticeably sharper (lower right panel). The hex pattern apparent in the images is the multi-fiber pattern inherent in the MCP structure and is an artifact of the fabrication process.

4. CORRECTING GEOMETRIC DISTORTIONS

Geometric distortion, also known as integral non-linearity (INL), is due to local variations in the plate scale of the detector. These variations are fixed in physical space and are due to small differences in the propagation speed of the anode and the structure of the MCPs themselves. The variations in the propagation speed are in turn due to local differences in the anode substrate thickness, anode trace resistivity, and the behavior of a charge cloud propagating along a complex network of conductive traces.

INL need only be calibrated once and then applied to all subsequent data sets after the data are converted to a CRF, as discussed in section 3.1. The INL for the COS detector is a slowly varying two-dimensional function of position (x and y). Except near the edges, where the distortion becomes highly non-linear, the INL has an amplitude of $<90 \mu\text{m}$ (15 pixels * $6 \mu\text{m}/\text{pixel}$), with a pixel-to-pixel variation of no more than 1.5%. The INL can be measured using a stainless steel mask with a fixed pattern of holes. The mask is placed in contact with the front MCP, illuminating the top MCP with light, and acquiring an image. The INL is characterized by comparing the known relative positions of the apertures with the measured positions in the digital space of the CRF.

For COS two masks were used. The primary mask has an



Figure 4: A portion of a slit image taken using the COS flight detector. The slits are 25 X 500 μm on 200 μm centers. Each row is separated by 2.5 mm.

array of 10 μm holes on 0.5 mm centers across the entire 85 x 10 mm active area of the MCP stack. The second mask has three rows of 25 x 500 μm slits on 200 μm centers with each row separated by 2.5 mm. Figure 4 is a portion of a slit image and Figure 5 shows the measured INL using the central row of slits for segment A of the COS detector.

4.1 Correcting for local variations (INL)

Correcting the INL in the detector is fairly straightforward process once the INL has been measured. To correct for the INL, first calculate the offset required to put the event back to the position where it should have been recorded in the absence of INL. In general, interpolating between the measured points in the INL calibration data is required to calculate the amount of INL for a given pixel. The location of an event in physical space is computed by subtracting the computed INL from the reported pixel location (see Equation 21).

$$P'_x = P_x - \text{INL}(P_x) \quad (21)$$

Figure 6 shows the edge of the COS detector before and after correction for INL. Notice how the multi-fiber boundary has an asymmetric aspect ratio prior to correction and a uniform aspect ratio after the correction, thus demonstrating that the geometric distortion has been successfully corrected.

5. CONCLUSIONS

We have presented two algorithms for correcting two types of distortions inherent in time-delay anode detectors. The first distortion is a global change in the plate scale of the detector and is due to temperature dependence in the anode substrate and integrating capacitor. This can be corrected using the electronic stims to track the change in plate scale and ultimately adjust the plate scale back to a common reference frame.

The second distortion occurs on local scales and is due to structures in the microchannel plates, electric field, and subtle variations in the propagation speeds and characteristics of the anode itself. Using images of fixed patterns to measure these variations it is possible to correct these effects. These two algorithms will be employed in the data reduction pipeline for the Cosmic Origins Spectrograph, a 4th generation Hubble Space Telescope instrument to be installed in 2003. See <http://cos.colorado.edu> for more details on the COS scientific mission and hardware development.

6. ACKNOWLEDGEMENTS

This work was supported by the Hubble Space Telescope Cosmic Origins Spectrograph program at the University of Colorado under contract NAS5-98043.

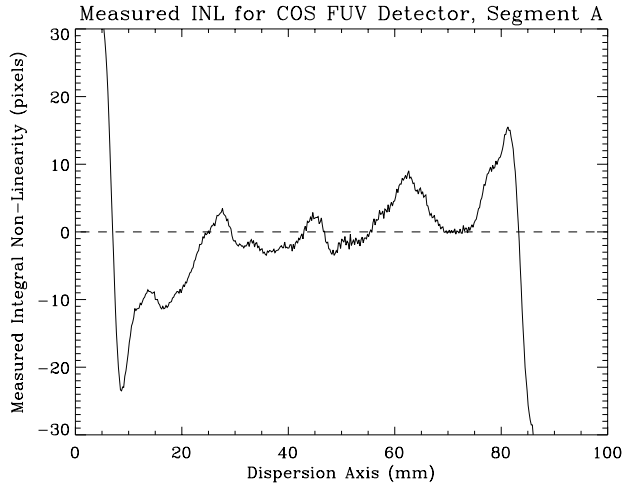


Figure 5: Measured integral non-linearity of a segment of the COS flight detector in the x (spectral) direction.

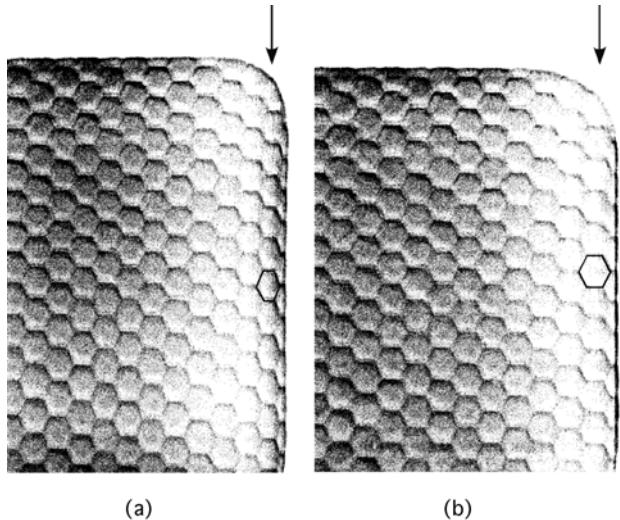


Figure 6: Demonstration of the INL correction. Panel (a) is an uncorrected image and panel (b) is the same image with the INL correction applied. Note the difference between the aspect ratio of the multi-fiber boundaries in the columns denoted by the arrows. Overlays of the multi-fiber boundaries are also shown to highlight the aspect ratio.

7. REFERENCES

- 1 O. H. W. Siegmund, R. F. Malina, K. Coburn, and D. Werthimer, "Microchannel plate EUV detectors for the Extreme Ultraviolet Explorer", IEEE Trans. Nucl. Sci., **NS-31**, 776-779 (1984).
- 2 J. M. Stock, O. H. W. Siegmund, J. S. Hull, K. E. Kromer, S. R. Jelinsky, H. D. Heetderks, M. L., and Lampton, S. B. Mende, "Cross-delay-line microchannel plate detectors for the Spectrographic Imager on the IMAGE satellite", Proc. SPIE, **3445**, 407-414 (1998)
- 3 O. H. W. Siegmund, *et al.*, "Delay-line detectors for the UVCS and SUMER instruments on the SOHO satellite", Proc. SPIE, **2280**, 89-100 (1994)
- 4 R. A. Kimble, *et al.*, "The on-orbit performance of the *Space Telescope Imaging Spectrograph*," in *Space Telescopes and Instruments V*, P. Y. Bely and J. B. Breckinridge, eds., Proc. SPIE, **3356**, 188-202 (1998).
- 5 O. H. W. Siegmund, M. Gummin, J. Stock, G. Naletto, G. Gaines, R. Raffanti, J. Hull, R. Abiad, T. Rodriguez-Bell, T. Magoncelli, P. Jelinsky, W. Donakowski, and K. Kromer, "Performance of the double delay line microchannel plate detectors for the Far Ultraviolet Spectroscopic Explorer", Proc. SPIE, **3114**, 283-294 (1997).
- 6 R. Indebetouw, R. McLean, E. Wilkinson, J. C. Green, and M. Beasley, "The hot carbon, oxygen, and nitrogen echelle spectrograph", Rev. Sci. Inst., **72**(3), 1850-1857 (2001).
- 7 R. A. Kimble, *et al.*, "In-flight performance of the MAMA detectors on the Space Telescope Imaging Spectrograph", Proc. SPIE, **3764**, 209-225 (1999).
- 8 G. M. Lawrence and W. E. McClintock, "Compact ultraviolet imaging microchannel plate detectors using CODEd anode converter (CODACON) readout systems", Proc. SPIE, **2831**, 104-111 (1996).
- 9 W. E. McClintock, C. A. Barth, R. E. Steele, G. M. Lawrence, and J. G. Timothy, "A rocket-borne instrument with a high-resolution microchannel plate detector for planetary ultraviolet spectroscopy", AO, **21**, 3071-3079 (1982).
- 10 E. Jenkins, *et al.*, "IMAPS - A high-resolution, echelle spectrograph to record far-ultraviolet spectra of stars from sounding rockets", Proc. SPIE, **932**, 213- (1988).
- 11 M. Lampton and C. W. Carlson, "Low-distortion resistive anodes for two-dimensional position-sensitive MCP systems", Rev. Sci. Inst., **50**, 1093-1097 (1979).
- 12 C. Firmani, E. Ruiz, C. W. Carlson, M. Lampton, and F. Paresce, "High resolution imaging with a two dimensional resistive anode photon counter", Rev. Sci. Inst, **53**, 570- (1982)
- 13 O. H. W. Siegmund, M. Lampton, J. Bixler, S. Chakrabarti, J. Vallerga, S. Bowyer, and R. F. Malina, "Wedge and strip image readout systems for photon-counting detectors in space astronomy", J. Opt. Soc. Am., **3**, 2139-2145 (1986)
- 14 J. S. Lapington, B. S. Sanderson, and L. B. Worth, "The verier electronic readout: high resolution and image stability form a charge division readout for microchannel plates", Proc. SPIE, **3445**, 535-545 (1998).
- 15 M. Lampton, O. H. W. Siegmund, and R. Raffanti, "Delay line anodes for microchannel-plate spectrometers", Rev. Sci. Inst., **58**, 2298-2305 (1987)
- 16 M. L. Lampton, O. H. W. Siegmund, and R. Raffanti, "Planar double-delay line readout technique for microchannel plate detectors", IEEE Trans. Nucl. Sci., **37**, 1548-1550 (1990).
- 17 O. H. W. Siegmund, M. A. Gummin, J. M. Stock, D. R. March, R. Raffanti, and J. Hull, "High-resolution monolithic delay-line readout techniques for two-dimensional microchannel plate detectors", Proc. SPIE, **2006**, 176-187 (1993)
- 18 H. W. Moos, *et al.*, "Overview of the *Far Ultraviolet Spectroscopic Explorer* Mission", ApJL, **538**, L1-L6 (2000).
- 19 J. A. Morse *et al.*, "Performance overview and science goals of the *Cosmic Origins Spectrograph* for the Hubble Space Telescope", Proc. SPIE., **3356**, 361-368 (1998).